The revised version of this paper is available at:
http://www.sciencedirect.com/science/article/pii/S001910351200406X

Extending MGS-TES Temperature Retrievals in the Martian Atmosphere up to 90 km: Retrieval Approach and Results

A. G. Feofilov[1,2], A. A. Kutepov[1,2], L. Rezac[3], M. D. Smith[4]

[1]{The Catholic University of America, 620 Michigan Ave., Washington D.C. 20064, USA}

[2]{NASA Goddard Space Flight Center, Code 674, Greenbelt, MD 20771, USA}

[3] {Hampton University, Hampton, VA, 23668, USA}

[4]{NASA Goddard Space Flight Center, Code 693, Greenbelt, MD 20771, USA}

Correspondence to: A. G. Feofilov (artem-feofilov@cua-nasa-gsfc.info)

Abstract

This paper describes a methodology for performing temperature retrievals in the Martian atmosphere in the 60–90 km altitude range using spectrally integrated 15 μm CO_2 limb emissions measured by the Thermal Emission Spectrometer (TES), the infrared spectrometer on-board the Mars Global Surveyor (MGS). We show that a limited number of limb-geometry sequences observed by this instrument are characterized by a high enough signal-to-noise ratio (SNR) to allow extending the upper limit of the retrievals to ~90 km. Using the methodology described in the paper, we have retrieved ~1200 individual temperature profiles from the MGS TES limb observations in the altitude range between 60 and 90 km. The set of retrieved temperature profiles is available for download in supplemental materials of this paper. The temperature retrieval uncertainties are mainly caused by noise in the observed radiance, and are estimated to be about 3 K at 60 km and below, 4 K at 70 km, 7 K at 80 km, 10 K at 85 km, and 20 K at 90 km. We compare the retrieved profiles to the Martian Year 24 (MY 24) dataset of the Mars Climate Database (MCD) and SPICAM measured temperature profiles for MY 27 and find good qualitative agreement. Quantitatively, our retrieved profiles are in general warmer and demonstrate strong profile-to-profile variability. The warm bias is explained by the selection of high SNR limb scans and can be estimated and taken into account (values in brackets below correspond to corrected TES). Overall, the average difference between the TES-retrieved temperatures and the MCD MY 24 dataset is: 7 (6) K at 60 km, 9 (7) K at 70 km, 10 (5) K at 80 km, and 13 (7) K at 90 km. The root-mean-square of the temperature variability caused by gravity waves estimated in this work is 7 K at 60 km, 8 K at 65 km, 11 K at 70 km, 15 K at 75 km, 18 K at 80 km, and 20 K at 85 km.

Keywords: temperature retrievals, middle atmosphere of Mars, remote sensing.

1. Introduction

The TES instrument on the MGS orbiter mapped the atmosphere of Mars for more than three Martian years allowing an unprecedented survey of the present Martian climate. The TES observations have been used to retrieve temperature profiles (Conrath et al. 2000), aerosol optical depth and physical properties (e.g. Pearl et al. 2001; Smith et al. 2001; Smith 2004; Clancy et al. 2003; Wolff and Clancy 2003), and water vapor abundance (Smith 2002; 2004). Most of the previously reported temperature retrievals from TES cover the atmosphere up to the ~0.01 mbar level, which corresponds to ~60 km altitude. The upper limit for the currently available TES retrievals was set in accordance with the signal-to-noise ratio of the observations used in the constrained linear inversion algorithm applied for temperature retrievals (Conrath et al., 2000). However, in the limb observation mode measurements were performed at higher altitudes, up to ~120 km altitude. In this work we used a forward-fitting temperature retrieval algorithm and applied it to a spectrally integrated CO_2 15 μm limb radiance to extend the upper altitude of temperature retrievals to 90 km and to provide high-altitude temperature data for Martian Years (MY) 24 and 25. Temperature soundings in the middle atmosphere of Mars are of great significance since they can give an important insight into the dynamics of the region that is linked with convective instabilities and gravity wave (GW) propagation and dissipation (e.g. Heavens et al., 2010 and references therein) and can provide additional constraints on tidal and gravity wave drag needed for modeling work (e.g. Forget et al., 1999; Forbes and Miyahara, 2006; Hartogh et al., 2007; McDunn et al., 2010; Medvedev et al., 2011; Bougher et al., 2011).

The structure of this paper is as follows: Section 2 describes the TES instrument. In Section 3 we discuss the specifics of the CO_2 15 μm emission in Martian atmosphere, define the integrated radiance that will be used for temperature retrievals, and introduce the radiance profile selection criteria. Section 4 describes the non-LTE code ALI-ARMS (see the Appendix for abbreviations not explained in the text), the temperature retrieval algorithm, and the retrieval uncertainties. In Section 5 we present the retrieved temperature profiles and compare them to averaged temperature profiles from the Mars Climate Database (MCD) dataset (Forget et al., 1999; Lewis et al., 1999; Gonzales-Galindo et al., 2005). A discussion of similarities and differences is also included into this section. Finally, we present our conclusions in Section 6.

2. TES instrument

MGS began mapping operations from Mars orbit on 1 March 1999 (MY 24, Ls = 104°) and provided nearly continuous monitoring of conditions in the Martian atmosphere for over three full Martian years. The MGS mission ended on 2 November 2006 when the contact with the spacecraft was lost. The TES instrument (Christensen et al. 2001) systematically measured and monitored the Martian surface and atmosphere throughout all phases of the mission. The imminent failure of a neon bulb required for calibration of the spectrometer forced spectrometer observations to end on 31 August 2004 (MY 27; Ls=81°), although observations continued using the TES bolometers. The near-polar solar-locked mapping orbit allowed 12 orbits per day of data at roughly 2:00 AM and 2:00 PM local time. A majority of observations were taken in the nadir geometry, but limb observations of the Martian atmosphere were included roughly every 10 degrees of latitude throughout the orbit (both day and night) throughout the mission. Each 8.3 mrad detector field-of-view had a projected size of about 13 km at the limb, allowing vertical resolution of just over a scale height. In a limb-geometry sequence, the 3x2 array of TES detectors scanned the atmosphere in overlapping steps from below the surface to about 120 km tangent height above the surface providing vertical sampling of about 1 to 5 km (see more details in (Christensen et al., 2001)). The total number of limb geometry spectra obtained during the mission is about 750,000. The spectral resolution of the TES instrument is 5 cm^{-1} and 10 cm^{-1}. In this work we used 10 cm^{-1} resolution spectra (Fig. 2). We show that a limited number of limb geometry spectra taken during the first two Martian years have SNR that allows an extension of temperature retrievals up to 90 km altitude. The selection criteria for these spectra are described in Section 3.2.

3. CO_2 15 μm radiance measured by TES

In the gas phase, carbon dioxide (CO_2) molecular vibrations involve combinations of symmetric stretch (ν_1), covalent bond bending (ν_2), and asymmetric stretch (ν_3) modes. The diagram in Fig. 1 shows the ground state and various excited vibrational levels of the main CO_2 isotope ($^{16}O^{12}C^{16}O$) up to an energy of 3900 cm^{-1}. The vibrational structure of minor isotopes is similar to that of the main isotope and is not shown in Fig. 1. The levels in Fig. 1 are marked in accordance with the Herzberg notation $\nu_1\nu_2^l\nu_3$ where ν_1, ν_2, and ν_3 denote the number of the corresponding vibrational quanta and the l symbol refers to the orbital quantum number. The 15 μm radiance measured by the TES instrument and used for temperature retrievals in this study arises from the optical transitions from vibrationally excited states with $\Delta\nu_2 = 1$, where $\Delta\nu_2$ denotes the change in the ν_2 vibrational quanta number.

3.1. $CO_2(\nu_2)$ vibrational levels populations in the Martian atmosphere

The interpretation of TES 15 μm limb radiance profiles requires knowing the populations of the corresponding $CO_2(\nu_2)$ vibrational levels at the altitudes of the limb observations. In general, in the lower atmosphere of planets the frequency of inelastic molecular collisions is sufficiently high that these collisions overwhelm other population/depopulation mechanisms of the molecular vibrational levels. This leads to a local thermodynamic equilibrium (LTE), and the populations follow the Boltzmann distribution governed by the local kinetic temperature. In the middle and upper atmosphere, where the frequency of inelastic collisions is much lower than that at lower altitudes, other processes also influence the vibrational levels population. These include: a) the direct absorption of solar radiance; b) absorption of the radiance coming from the lower atmosphere; c) radiative de-excitations; d) vibrational-translational (V–T) energy exchanges by collisions with molecules and atoms of other atmospheric constituents; and e) collisional vibrational-vibrational (V–V) energy exchange with other molecules. As a result, LTE no longer applies in this altitude region and the populations must be found by solving the self-consistent system of kinetic equation and radiative transfer equation, which express the balance relations between various excitation/de-excitation processes described above. Our calculations show that for the $CO_2(\nu_2)$ vibrational levels in the Martian atmosphere the LTE-breakdown is observed at heights greater than ~80 km and that $CO_2(\nu_2)$ populations depend mainly on the balance between processes b) – e) and the most important rate coefficient that influences the population of $CO_2(\nu_2)$ vibrational levels in the upper atmosphere of Mars is $k_{VT}\{CO_2\text{-}O\}$, the quenching rate coefficient for V–T energy exchange process at CO_2–O collisions (Feofilov et al, 2011 and references therein). The sensitivity of the retrieval to this coefficient will be discussed below.

3.2. TES spectra selection and processing

In this work we used a spectrally integrated 15 μm CO_2 band radiance in the retrievals to increase SNR and to extend the upper limit of the retrieved temperature profile. In a sense, using the integrated radiance converts the spectrometer to a broadband radiometer like, for example, the SABER instrument (Russell et al., 1999) that was successfully used for temperature retrievals in the Earth's atmosphere up to ~110 km altitude from the 15 μm broadband radiance profiles. Spectra selection for integration and processing was based on two criteria: a limb sequence should a) provide a sufficient number of measured points above 60 km altitude and b) SNR for the integrated signal should be greater than unity up to at least 85 km. The calculations performed in this work show that both during the day and night in the Martian atmosphere, the 15 μm CO_2 band radiance is confined within the 560–770 cm^{-1} spectral range. Below we will refer to this range as to "spectral window A". Besides this window, we have also defined windows B (510–560 cm^{-1}) and C (770–830 cm^{-1}) that were used to estimate the noise and offset in the observed signal. The calculations show that all spectral line intensities in windows B and C are less than 1% of the line intensities in the maximum of the 15 μm manifold. For the purpose of the present work we fit for a second order polynomial using the spectral points in windows B and C, and then subtract the corresponding offset values from the spectral intensities in window A. Examples of the resulting spectra in the 61–89 km altitude interval are shown in Fig. 2a–f. As one can see, the suggested procedure efficiently removes the offsets at all considered altitudes.

The integrated values of the 15-μm radiance in the 560–770 cm^{-1} spectral range with offset removed are shown in Fig. 2g. This panel also contains the NER (noise equivalent radiance) value estimated from windows B and C. As one can see in Fig. 2g, for a given limb sequence the NER becomes comparable to the integrated signal at ~86 km altitude. The number of measurements for which the NER allows retrievals up to 90 km altitude is small compared with the total number of limb measurements. There are two reasons for that. First, the altitude coverage of limb measurements differs and not all limb sequences provide valid data points up to 90 km altitude. Second, the increasing noise in TES observations as the mission went on limited the limb scans with "good SNR" up to 90 km to the first two Martian years of the mission. We also note that selecting high SNR scans may introduce a positive offset to the average retrieved temperature profile as we will show below in Sect. 5.2. However, the selection routine does not modify any individual temperature profile used in the study nor does it add to the retrieval errors. We will estimate the systematic error caused by the high SNR scan selection in Sect. 5.2. Overall, we have identified 1410 limb sequences that satisfy the SNR and altitude coverage criteria. The latitudinal/seasonal distribution of the selected measurements is presented in Fig. 3. As one can see, most of the selected observations correspond to nighttime cases. This needs some explanation. The day-night temperature difference at 85 km altitude due to diurnal thermal tide is ~7 K (McCleese et al., 2008) and the expected 15 μm radiance increase due to that temperature change is ~20%. Another 15–20% increase in 15 μm radiance comes from the redistribution of the absorbed solar energy (see Fig. 1). However, this 40% radiance increase is compensated by the higher daytime TES noise level that leads to filtering out more measurements during daytime than during nighttime.

All of the selected limb sequences were processed using the retrieval procedure described in the next section.

4. ALI-ARMS research code and retrieval algorithm

4.1. ALI-ARMS research code

All of the calculations performed in this work were made using the ALI-ARMS computer code (see Kutepov et al., 1998; Gusev, 2003; Gusev and Kutepov, 2003; and references therein) that solves the multi-level problem using the Accelerated Lambda Iteration (ALI) technique developed for calculating non-LTE populations of atomic and ionic levels in stellar atmospheres (Rybicki and Hummer, 1991). The code iteratively solves a set of statistical equilibrium equations and the radiative transfer equation. The algorithm efficiency is ensured by the ALI technique, which avoids the expensive radiative transfer calculations for the photons trapped in the optically thick cores of spectral lines. The ALI-ARMS model was successfully applied by Kaufmann et al. (2002; 2003) and Gusev et al. (2006) to the non-LTE diagnostics of spectral observations of the Earth's limb from the CRISTA instrument (Offermann et al., 1999; Grossmann et al., 2002). Kutepov et al. (2006) used ALI-ARMS to validate temperature retrievals from the 15 μm CO_2 emissions measured by the SABER instrument onboard the terrestrial TIMED satellite. This code was also used for the H_2O non-LTE model validation (Feofilov et al., 2009) and for the $k_{VT}\{CO_2\text{-}O\}$ rate coefficient estimate from the atmospheric observations (Feofilov et al., 2011 and references therein).

In this work we used the CO_2 non-LTE model developed in our group (Gusev, 2003; Kutepov et al., 2006). The full model includes 350 vibrational levels of 7 CO_2 isotopes but as Gusev (2003) showed, for most of the applications it is enough to include five CO_2 isotopes, 60 vibrational levels, and 20,000 optical transitions from the HITRAN 2004 database (Rothman et al. 2005) so we used this optimized model The retrieval method implemented in the ALI-ARMS code is similar to the iterative onion-peel technique using the relaxation method described in Gordley and Russell (1981) for LTE. We will describe here the algorithm for non-LTE temperature retrieval but this approach is applicable also for trace gas retrievals. The process starts with the initial temperature profile combined with pressure, VMRs of CO_2 and atomic oxygen distributions taken from the MCD. The non-LTE populations are estimated and used for monochromatic limb radiance calculations. These radiances are integrated for each limb path and an integrated profile is convolved with the TES field of view. The resulting simulated radiance I is compared to the measured radiance at each tangent height, and the temperature profile is iterated using the following relaxation scheme: $T_{i+1} = T_i + (I_{meas} - I_i)/(\partial I / \partial T)$ where T_{i+1} and T_i are the temperature values at the $i+1$-th and i-th iterations, respectively, I_{meas} is the integrated limb radiance measured by TES (see Section 3.2 above), I_i is the simulated limb radiance at the i-th iteration, and $(\partial I / \partial T)$ is the numerically calculated derivative of the radiance produced by the forward model with respect to temperature. Finally, a new temperature profile is produced, pressure profile is adjusted using the hydrostatic law, the new non-LTE populations of CO_2 molecular levels are calculated, and the radiance is simulated again. The iterations are repeated until the differences between the simulated and measured radiances become equal to or smaller than the radiance noise in the observed integrated limb radiance. It is important to note that if iteration is allowed to proceed indefinitely, then it will converge to an "undesirable exact solution" or quickly is getting unstable (Houghton et al, 1984, p.148). However, a convergence analysis demonstrates that broad-scale features converge rapidly, and the fine-scale features (often associated with the signal noise) converge slowly, so the reasonable "physical solution" may be found if the iteration is stopped at the right point (see below).

In this work we ran the retrievals up to 100 km altitude even though the estimates show that the upper limit for SNR=1 in TES temperature retrievals is 90 km. This was done deliberately. Even though the individual radiance values in 90–100 km layer are comparable to NER, the integrated radiance of the layer has SNR larger than 1 and, therefore, still carries the information about the area. Temperature values retrieved in this layer combined with the model temperature profile above ensure proper radiance add-on for the line-of-sight of the instrument in limb observation mode. These temperatures cannot be considered as true ones since they compensate for the difference between the model atmosphere and the real one above 100 km. However, as a result of using the 90–100 km layer the temperature retrievals below are less affected by the uncertainties of the atmosphere above (see the self-consistency tests in the next section).

4.2. Self-consistent retrievals, convergence of the method, and retrieval uncertainties

To illustrate the convergence of the method we have performed a self-consistent retrieval using 10 Martian atmospheric profiles corresponding to seasons and latitudes shown in Fig. 25 and Fig. 28 of (Kleinböhl et al., 2009). We have selected three representative cases for demonstrational purposes. Atmosphere #1 corresponds to tropical case (latitude = 0°) and the atmospheres #2 and #3 represent high latitudes in the Northern and Southern hemispheres, respectively (latitude = 80°N and 80°S) for L_s=330–340°. Temperature distributions up to 0.01 Pa level were taken from (Kleinböhl et al., 2009) and supplemented with the MCD atmospheric profiles available for download at http://johnson.lmd.jussieu.fr:8080/las/servlets/dataset. We used pressure/temperature, CO_2, and O VMR profiles covering the 0–200 km altitude range. To simulate the GW-induced temperature variations we combined the average temperature deviations for the corresponding models from (Kleinböhl et al., 2009) with the temperature variations estimated from the RMS wind values from (Medvedev et al., 2011) above 0.01 Pa level assuming the proportionality of these parameters (Medvedev, private communication, 2012). As a result, we obtained the temperature RMS profile $\langle \Delta T(z) \rangle$ up to the turbopause altitude. Then we "generated" a GW for each test atmosphere by combining two harmonics with random wavelengths and phases (17 and 25 km for the examples shown in Fig. 4). The GW amplitude was modulated by $\langle \Delta T(z) \rangle \cdot \sqrt{2}$ producing waves with up to ±35 K amplitude at 85–100 km. The "random" pattern of the wave was kept the same for all cases to simplify tracing noise induced effects in retrieved temperatures. The obtained waves were applied to the corresponding average temperature distributions. The top of the atmosphere (TOA) was set at 200 km, and $k_{VT}\{CO_2\text{-}O\}$ was set to $6\cdot10^{-12}cm^3s^{-1}$, the value that is typically retrieved from the atmospheric observations on Earth (Sharma and Wintersteiner, 1990; Ratkowski et al., 1994; Gusev et al., 2006; Feofilov et al., 2011). First, we calculated the non-LTE populations of the CO_2 vibrational levels at all heights and then calculated the limb radiance for each spectral line in window A and at each tangent height. After that, the radiance was spectrally integrated, convolved with the vertical field of view (FOV) of the TES instrument, and the resulting integrated 15 µm radiance formed the reference profile $I_{ref}(z)$ for the corresponding atmospheric model. Three retrievals were performed for each of the test atmospheres: two noise-free retrievals that started from temperature profiles that were 25 K warmer and colder than the original one, and one retrieval starting from the 25 K warmer profile with noise added to the reference radiance. The noise was estimated from real TES spectra for the corresponding season and locations using spectral information in windows B and C. The hydrostatic adjustment of the pressure-temperature profile was performed at each of the iterations as it is done in the standard ALI-ARMS temperature retrieval process. It is convenient to define an additional convergence criterion for the retrieval process as a weighted relative radiance deviation in the 60–90 km altitude range: $(\Delta I_i / I)_{R.M.S.} = \left[\sum_{id=60}^{90} ((I_{ref}^{id} - I_i^{id}) / I_{ref}^{id})^2 / (90-60+1) \right]^{1/2}$ where I_{ref}^{id} is a "reference" limb radiance for tangent height *id* and I_i^{id} is the radiance simulated at the i-th iteration for the same tangent height. We remind here that in real retrievals the reference radiance profile $I_{ref}(z)$ is substituted with measured radiance profile $I_{meas}(z)$. The behavior of $(\Delta I / I)_{R.M.S.}$ for all three test atmospheres is shown in Fig. 4a. As one can see, noise-free retrievals demonstrate rapid convergence up to the 6–7th iteration. After that the convergence continues but at a slower rate. The corresponding temperature profiles obtained at the 11th iteration are close to the original profile (see the temperature deviation from the original profile in Fig. 4b–d). However, further iterations do not lead to better agreement between the retrieved and original profiles. This is explained by a) large vertical FOV of the instrument that "mixes" the effects of different heights; b) hydrostatic adjustment that redistributes the changes occurring in the lower part to the whole atmosphere. Overall, the uncertainties caused by the retrieval methodology are within ± 4K limits for all three test atmospheres. One can trace the GW-induced temperature variation pattern (beating frequency) in the residuals in Fig. 4b–d but its magnitude is less than 1 K at heights up to 90 km. Naturally one should expect larger errors in retrieving GWs with a wavelength shorter than doubled value of FOV. Adding noise complicates the situation. The convergence becomes slower (see the corresponding solid lines with circles in Fig. 4a) and there is almost no improvement in $(\Delta I / I)_{R.M.S.}$ after the 6th iteration (the NER level is reached). Solid lines with circles in Fig 4b–d show the discrepancy between the retrieved temperature profile and the reference one for the 6th iteration. Note the similarity of the response of all three retrievals to adding the same noise pattern to the reference radiance profile.

Another important factor that might affect the retrievals is the uncertainty of the atmospheric profile below and above the retrieval area. The lower part may affect the retrieval through hydrostatics while the upper part may change the absorption and emission along the line of sight in the limb observation mode. To estimate these effects we performed a set of retrievals for the same three model Martian atmospheres. For simplicity, we demonstrate them on noise-free, GW-free retrievals starting from the original temperature distributions. For these tests we only changed the temperature profiles above and below the retrieval area by ±20 K and ±5 K, respectively. All the other combinations (0 K change below 50km, ±20 K above 100 km and so on) have demonstrated smaller effects on the retrieval and are not shown here. Figure 5 demonstrates that ±5 K changes below 50 km altitude do not significantly affect the retrievals in 50–90 km area (overall offset caused by these changes is less than ±1 K). On the other hand, ±20 K modification of temperature profile above 100 km leads to ±6 K offsets at 90 km altitude for Atmosphere #3 and smaller offsets for other two test atmospheres.

Changing $k_{VT}\{CO_2\text{-}O\}$ to $1.5\cdot10^{-12}cm^3s^{-1}$, the value obtained in laboratory measurements (Pollock et al., 1993; Khvorostovskaya et al., 2002; Castle et al., 2006; Huestis et al., 2008) modifies the retrieved profile in the entire range of the retrieval. This is explained by the non-LTE effects in CO_2: reducing the collisional rate coefficient leads to less efficient thermalizing of the vibrational levels that become more populated by radiance coming from the warmer and denser layers below. This leads to overestimating the radiance and, therefore, to underestimating the temperature. The temperature uncertainty caused by the $k_{VT}\{CO_2\text{-}O\}$ change from “atmospheric” to “laboratory” value is about 3 K above 65 km. Finally, “removing” the 110–200 km part of the atmosphere (TOA 110 in Fig. 5) doesn’t significantly affect the 60–90 km retrieval area since missing radiance is compensated in the retrieval process by increasing the temperature in the 90–100 km layer. However, lowering TOA introduces positive offset so we opted not to lower TOA. Overall, running the retrievals with random noise profiles and summing up all the uncertainties listed in this section provides the following estimate for the uncertainty of the single profile retrieval: 3 K at 60 km, 4 K at 75 km, 7 K at 80 km, and 10 K at 85 km altitude.

5. Temperature retrievals from TES measurements

5.1. Input data and retrieval procedure

All the retrievals performed in this study utilized the retrieval algorithm described in Section 4. For each of the 1410 integrated TES radiance profiles (see Section 3.2 and Fig. 3) the initial guess atmospheric profile was assembled from pressure/temperature profiles in the 10–60 km altitude range retrieved by the TES team using nadir geometry observations (Conrath et al. 2000; Smith 2004), and from pressure/temperature, CO_2 and O VMRs taken from the MCD in the 60–200 km interval. The retrieval was performed over the 50–100 km range. The upper 10 km layer of this interval was used to damp the effects of uncertainties in the upper atmosphere (see Section 4.2) and is included in the retrieved temperature dataset only for quality control purposes (the larger the gradient in the 90–100 km layer, the lager the difference between the model atmospheric profile above 100 km, and the real one). The 50–60 km interval was included in the retrieval to allow for temperature profile adjustment in this area due to changes in the upper part. The retrieval procedure was described in Sect. 4.1. For the majority of the profiles the $(\Delta I / I)_{R.M.S.}$ calculated for 60–90 km altitude range reached the value calculated with the corresponding NER (estimated using windows B and C) between the 7th and 10th iteration. Approximately 14% of the processed profiles were filtered out due to poor convergence (compare small filled and large empty circles and triangles in Fig. 3).

In the next section we present 1214 temperature profiles that satisfied these convergence criteria.

5.2. Retrieved temperature profiles

The complete set of individual temperature profile retrievals is available for download as an archive at http://cua-nasa-gsfc.info/feofilov/TES_HighAlt.zip or in the supplemental materials of the online version of the paper. For a description of the dataset see the file "readme.txt" inside the archive. In this work we present some examples of individual retrievals and compare the averaged profiles with those from the MCD (using the standard MY 24 dust and average flux scenario) and with temperature distributions obtained from stellar occultation observations by the SPICAM instrument discussed in (Forget et al., 2009).

Three examples of individual temperature profiles retrieved from integrated TES radiance are shown in Fig. 6a–c. Below ~55 km the retrievals match the initial temperature profile. Above 60 km, the retrieved temperature profiles differ from the original MCD profile and, in general, individual temperature retrievals show much higher variability than the model profiles. This may be explained by gravity waves in the Martian atmosphere, which are not present in the averaged model dataset.

Lack of temperature measurements in the Martian atmosphere for the period considered in the study hinders a direct profile-by-profile comparison with other instruments. Therefore, we compare the TES temperature retrievals with the MCD MY 24 simulations for the corresponding seasons and with the SPICAM temperature for MY 27. For the MCD comparison we used the zonally and seasonally (with a 30° step over L_s) TES-retrieved temperatures. MCD temperature distributions were averaged over the same period and for the same latitudinal belt and local time. For SPICAM comparison we took the MY 27 dataset described in (Forget et al., 2009), which were retrieved for top temperature of 175 K (top temperature value does not affect the SPICAM retrievals below 110 km). It is important to note here that these retrievals do not depend on non-LTE effects since the SPICAM instrument observes the atmosphere in occultation mode and its high spectral resolution allows tracking only the transitions from the ground state whose population can be considered to be equal to the total CO_2 density.

Figure 7 shows six panels which correspond to six latitudinal/seasonal "boxes" defined in Fig. 3. In this figure we compare MGS-TES retrievals for MY 24 with MCD simulated profiles and SPICAM measured temperature distributions for MY 27. Figure 8 demonstrates the MY 24 and MY 25 temperature retrieval comparisons with MCD temperatures. The profiles are marked in the figure captions with L_s counted from the year the mission started (MY 24) so that L_s=390° corresponds to MY 25, L_s=30°. The SPICAM distributions in Fig. 7 are shown down to ~60 km, the altitude below which the airborne dust leads to overestimating the retrieved temperatures (Quemeralis et al., 2006; Forget et al., 2009). The bins for the TES data correspond to SPICAM bins. Error bars for SPICAM in the 60–90 km layer are almost constant and are equal to ± 10K. They are not shown for the readability of the figure. Lines with empty circles in Fig. 7 and Fig. 8 show standard variability of TES-retrieved temperatures in the considered bin. Error bars for individual TES temperature retrievals are given at the end of Sect. 4.2. The number of averaged TES profiles is indicated in figure caption.

As one can see, there is a qualitative agreement between the TES, SPICAM, and the MCD temperature profiles. However, the absolute temperature values differ. In general, MGS retrieves higher than MCD and SPICAM retrieves lower temperatures than MCD above ~80 km. An analysis of our entire retrieval set in comparison to the MCD profiles for the same seasons and locations gives the following values for the offset: 7 K at 60 km, 8 K at 65 km, 9 K at 70 km, 10 K at 75 km, 10 K at 80 km, 11 K at 85 km, and 13 K at 90 km. One can also note large variability for TES-retrieved temperature distributions. This is expected since our TES retrievals represent individual profiles while the MCD profiles do not represent GW variability. The increase of TES profiles variability with altitude can be explained by the growth of GW amplitudes in the Martian atmosphere (Fritts et al., 2006). Accounting for the noise-induced variability, one obtains the following values for the RMS of vertical temperature variability caused by GW: 7 K at 60 km, 8 K at 65 km, 11 K at 70 km, 15 K at 75 km, 18 K at 80 km, and 20 K at 85 km. This is comparable with the RMS of GW amplitude inferred from MCS observations and wind RMS (see Sect. 4.2).

Let us consider possible reasons for the positive temperature offset. First, there might be deviations of the real atmospheric conditions for a given period from that modeled by the GCM and measured by SPICAM 3MY later. It is known that there were at least two major dust storm events during the considered time period (Smith, 2004): one at L_s=225° and one at L_s=260° that might be the cause for large temperature deviation shown in Fig. 7d. Second, the retrieval algorithm and non-LTE model uncertainties may be partially responsible for the offset (see Sect. 4.2). Third, the offset may be caused by radiance calibration issues like the vertical field of view wing shape or by the spectra selection procedure (see Sect. 3.2). A radiance leak from below would be barely noticeable if the vertical radiance gradients are low. However, if an area with low temperatures and pressures is observed then the contributions of lower layers become important (Rezac, 2011). And last but not least, positive offset in our TES retrievals can be linked with the limb sequence selection criteria described in Sect. 3.2 since using a selecting procedure that discards the observations with low SNR may filter out the low temperature cases that are characterized by low radiance values. We consider this as the most probable source of the observed systematic offset. To estimate its value we performed the following study. For each of the time periods and locations shown in Fig. 7 we have built a distribution of SNR maximal height using all available TES data. The maxima of these distributions are centered at individual heights $H_{SNR=1}$ that are lower than 85 km SNR=1 cutoff used for scans selection. The typical values of $H_{SNR=1}$ are about 70 km and the difference between $H_{SNR=1}$ and 85 km can be used for characterizing the temperature offset introduced by our scan selection criteria. Calculations performed with the help of ALI-ARMS show that the temperature change required to compensate for low SNR at 85 km depends on the atmospheric scenario and varies from 2 K to 4 K per 1 km of (85 – $H_{SNR=1}$) difference. The corresponding values are given in Fig. 7 and Fig. 8 legends. We assume that the temperature profile variability is caused mainly by gravity waves that penetrate these heights in Martian atmosphere (Medvedev et al., 2011 and references therein) and that the scan selection routine only picks up "positive" waves with respect to average temperature profile. Therefore, we assigned the estimated temperature offset to 85 km with a linear decrease down to 50 km altitude. Solid curves with triangles in Fig. 7 and Fig. 8 show the average temperature distributions compensated for scan selection effects.

As one can see, in 11 cases out of 12 shown in Fig. 7 and Fig. 8 the suggested correction leads to better agreement between the MCD and TES retrievals above ~60 km and the averaged temperature offset reduces to 6 K at 60 km, 7 K at 65 km, 7 K at 70 km, 6 K at 75 km, 5 K at 80 km, 6 K at 85 km, and 7 K at 90 km.

6. Conclusion

We have described a non-LTE model and algorithm that is applied to retrieve temperature profiles in the Martian atmosphere using the 15 μm limb geometry CO_2 emissions measured by the TES instrument. We used integrated limb radiance in the 560–770 cm^{-1} spectral range to increase the SNR and to extend the retrievals up to ~90 km altitude. We showed that the temperature retrieval algorithm provides a stable solution. The combined uncertainty of the temperature retrieval due to noise, non-LTE model uncertainties, vertical FOV averaging, and algorithm properties for a single retrieval is estimated to be 3 K at 60 km and below, 4 K at 70 km, 7 K at 80 km, 10 K at 85 km, and 20 K at 90 km altitude. Overall, ~1200 individual limb sequences have been selected, processed, and provided for download. The temperature profiles retrieved from TES at 60 – 90 km altitude were compared to corresponding profiles obtained from the Mars Climate Database and from the SPICAM observations. In general, a good qualitative agreement between the datasets is observed. A positive offset of the TES retrieved temperatures with respect to the MCD temperatures was found that varies from 7 K at 60 km to 13 K at 90 km. We explain this offset both by natural atmospheric variability and by the filtering out of some of the low temperature profiles in our signal selection routine. Compensating for the high SNR scan selection reduces the difference between TES and MCD to 6 K at 60 km, 7 K at 65 km, 7 K at 70 km, 6 K at 75 km, 5 K at 80 km, 6 K at 85 km, and 7 K at 90 km. The RMS of the gravity wave amplitude estimated from the TES retrievals performed in this work is 7 K at 60 km, 8 K at 65 km, 11 K at 70 km, 15 K at 75 km, 18 K at 80 km, and 20 K at 85 km. In summary, this study extends the limits of the already highly capable TES instrument, and validates the general concepts built in to the Martian GCMs.

Acknowledgements

The work of A. Feofilov and A. Kutepov was supported by NASA grant NNX08AL12G. The authors are grateful to two anonymous reviewers for their thorough analysis of the manuscript and their helpful comments and recommendations. We also thank Dr. Francois Forget for providing the SPICAM data and consultations regarding usage of the MCD data.

Appendix: Abbreviations used in text

ALI-ARMS: Accelerated Lambda Iterations for Atmospheric Radiation and Molecular Spectra

CRISTA: CRyogenic Infrared Spectrometers and Telescopes for the Atmosphere

FOV: field of view

GCM: General Circulation Model

GW: Gravity Wave

HITRAN: HIgh-resolution TRANsmission molecular absorption database

LTE: Local Thermodynamic Equilibrium

MGS: Mars Global Surveyor

MY 24: Martian Year 24

NER: Noise Equivalent Radiance

RMS: Root Mean Square

SABER: Sounding of the Atmosphere using Broadband Emission Radiometry

SNR: Signal to Noise Ratio

TOA: Top of the Atmosphere

TES: Thermal Emission Spectrometer

TIMED: Thermosphere Ionosphere Mesosphere Energetics and Dynamics

VMR: Volume Mixing Ratio

References

Bougher, S. W., T. M. McDunn, J. Murphy, and M. Chizek, Coupling of Mars Lower and Upper Atmosphere Revisited: Impacts of Gravity Wave Momentum Deposition on Upper Atmosphere Structure, Mars Modeling and Observations Workshop, Extended Abstracts, 370–373, Paris, France, 8–11 February, 2011.

Castle, K. J., K. M. Kleissas, J. M. Rhinehart, E. S. Hwang, and J. A. Dodd, Vibrational relaxation of $CO_2(\nu_2)$ by atomic oxygen, J. Geophys. Res., 111, A09303, doi:10.1029/2006JA011736, 2006.

Christensen, P. R., J. L. Bandfield, V. E. Hamilton, S. W. Ruff, H. H. Kieffer, T. N. Titus, M. C. Malin, R. V. Morris, M. D. Lane, R. L. Clark, B. M. Jakosky, M. T. Mellon, J. C. Pearl, B. J. Conrath, M. D. Smith, R. T. Clancy, R. O. Kuzmin, T. Roush, G. L. Mehall, N. Gorelick, K. Bender, K. Murray, S. Dason, E. Greene, S. Silverman, and M. Greenfield, Mars Global Surveyor Thermal Emission Spectrometer experiment: Investigation description and surface science results, J. Geophys. Res., 106(E10), 23,823–23,871, 2001.

Clancy, R.T., M.J. Wolff, P.R. Christensen. Mars aerosol studies with the MGS TES emission phase function observations: optical depths, particle sizes, and ice cloud types vs latitude and solar longitude. J. Geophys. Res., 108, doi:10.1029/2003JE002058.

Conrath, B. J., J. C. Pearl, M.D. Smith, W. C. Maguire, S. Dason, M. S. Kaelberer, and P. R. Christensen, Mars Global Surveyor Thermal Emission Spectrometer (TES) observations:

Atmospheric temperatures during aerobraking and science phasing, 2. Geophys. Res., 105, 9509–9520, 2000.

Feofilov, A.G., Kutepov, A.A., Pesnell, W.D., Goldberg, R.A., Marshall, B.T., Gordley, L.L., García-Comas, M., López-Puertas, M., Manuilova, R.O., Yankovsky, V.A., Petelina, S.V., and Russell III, J. M., Daytime SABER/TIMED observations of water vapor in the mesosphere: retrieval approach and first results, Atmos. Chem. Phys., 9, 8139–8158, 2009.

Feofilov, A.G., A. A. Kutepov, C.-Y. She, A. K. Smith, W. D. Pesnell, and R. A. Goldberg: $CO_2(\nu_2)$-O quenching rate coefficient derived from coincidental SABER/TIMED and Fort Collins lidar observations of the mesosphere and lower thermosphere, Atmos. Chem. Phys. Discuss., 11, 32,583–32,600, 2011.

Forbes, J.M., Miyahara, S., Solar semidiurnal tide in the dusty Mars atmosphere. J. Atmos. Sci. 63(7), 1798–1817, 2006.

Forget, F., Hourdin, F., Fournier, R., Hourdin, C., Talagrand, O., Collins, M., Lewis, S.R., Read, P.L., Huot, J.-P., Improved general circulation models of the martian atmosphere from the surface to above 80 km. J. Geophys. Res. 104, 24,155–24,176, 1999.

Forget, F., Montmessin, F., Bertaux, J.-L., Gonzalez-Galindo, F., Lebonnois, S., Quemerais, E., Reberac, A., Dimarellis, E., Lopez-Valverde, M.A.: Density and temperatures of the upper Martian atmosphere measured by stellar occultations with Mars Express SPICAM, J. Geophys. Res., 114(E01004), doi:10.1029/2008JE003086, 2009.

Fritts, D. C., L. Wang, and R. H. Tolson, Mean and gravity wave structures and variability in the Mars upper atmosphere inferred from Mars Global Surveyor and Mars Odyssey aerobraking densities, J. Geophys. Res., 111(A12304), doi:10.1029/2006JA011897, 2006.

Gonzalez-Galindo, F., Lopez-Valverde, M.A., Angelats i Coll, M., Forget, F.: Extension of a Martian general circulation model to thermospheric altitudes: UV heating and photochemical models, J. Geophys. Res. 110(E09008), doi:10.1029/2004JE002312, 2005

Gordley, L.L and J.M. Russell III, Rapid inversion of limb radiance using an emissivity growth approximation, Appl. Opt. 20, 807–813, 1981.

Grossmann, K. U., Offermann, D., Gusev, O., Oberheide, J., Riese, M., and Spang, R.: The CRISTA-2 mission, J. Geophys. Res., 107(D23), 8173–8185, doi:10.1029/2001JD000667, 2002.

Gusev O.A.: Non-LTE diagnostics of infrared observations of the planetary atmospheres. Ph.D. thesis, University of Munich, http://deposit.ddb.de/cgi-bin/dokserv?idn=968893651&dok_var=d1&dok_ext=pdf&filename=968893651.pdf, 2003.

Gusev, O., Kaufmann, M., Grossmann, K.U., Schmidlin, F.J., and Shepherd, M.G.: Atmospheric neutral temperature distribution at the mesopause/turbopause altitude, J. Atmos. Sol.-Terr. Phy., 68(15), 1,684–1,697, doi:10.1016/j.jastp.2005.12.010, 2006.

Gusev, O.A. and Kutepov, A.A.: Non-LTE gas in planetary atmospheres, in book: Stellar Atmosphere Modeling, I.Hubeny, D.Mihalas, and K.Werner, Eds., ASP Conference Series, 288, 318–330, 2003.

Hartogh, P., Medvedev, A.S., Jarchow, C., Middle atmospheric polar warmings on Mars: Simulations and study on the validation with submillimeter observations, Adv. Space Res. 55, 1103–1112, 2007.

Heavens, N. G., M.I. Richardson, W.G. Lawson, C. Lee, D.J. McCleese, D.M. Kass, A. Kleinböhl, J.T. Schofield, W.A. Abdou, J.H. Shirley, Convective instability in the martian middle atmosphere, Icarus, 208, 574–589, 2010.

Houghton, J.T., Taylor, F.W., and Rodgers, C.D, Remote soundings of atmospheres, Cambridge University Press, Cambridge, New York, Series title: Cambridge planetary science series, 343 pp, 1984, republished 2009.

Huestis, D. L., S. W. Bougher, J. L. Fox, M. Galand, R. E. Johnson, J. I. Moses, J. Pickering, and R. V. Yelle, Cross Sections and Reactions Rates for Comparative Planetary Aeronomy, Space Sci. Reviews, 139, 63–105, doi:10.1007/s11214-9383-7, 2008.

Kaufmann, M., Gusev, O.A., Grossmann, K.U., Roble, R.G., Hagan, M.E., Hartsough, C., and Kutepov, A.A.: The vertical and horizontal distribution of CO_2 densities in the upper mesosphere and lower thermosphere as measured by CRISTA, J. Geophys. Res., D107, 8182, 10.1029/2001JD000704, 2002.

Kaufmann, M., Gusev, O.A., Grossmann, K.U., Martin-Torres, F.J., Marsh, D.R., and Kutepov, A.A.: Satellite observations of day- and nighttime ozone in the mesosphere and lower thermosphere, J. Geophys. Res., 108D, 10.1029/2002JD002800, 2003.

Khvorostovskaya, L. E., I.Yu. Potekhin, G.M. Shved, V.P. Ogibalov, and T.V. Uzyukova, Izvestiya Atmos. Ocean. Phys., 38, 613–624, 2002.

Kleinböhl, A., Schofield, J.T., Kass, D.M., Abdou, W.A., Backus, C.R., Sen, B., Shirley, J.H., Lawson, W.G., Richardson, M.I, Taylor, F.W., Teanby, N.A., McCleese, D.J.: Mars Climate Sounder limb profile retrieval of atmospheric temperature, pressure, and dust and water ice opacity, J. Geophys. Res., 114(E10006), doi:10.1029/2009JE003358, 2009.

Kutepov, A.A., Gusev, O.A., and Ogibalov, V.P.: Solution of the non-LTE problem for molecular gas in planetary atmospheres: Superiority of accelerated lambda iteration, J. Quant. Spectrosc. Ra., 60, 199–220, 1998.

Kutepov, A.A., Feofilov, A.G., Marshall, B.T., Gordley, L.L., Pesnell, W.D., Goldberg, R.A., and Russell, J.M., III: SABER temperature observations in the summer polar mesosphere and lower thermosphere: importance of accounting for the CO_2 ν_2-quanta V–V exchange, Geophys. Res. Lett., 33, L21809, doi:10.1029/2006GL026591, 2006.

Lewis, S.R., Collins, M., Read, P.L., Forget, F., Hourdin, F., Fournier, R., Hourdin, C., Talagrand, O., Huot, J.-P.: A climate database for Mars, J. Geophys. Res. Planets, 104(10), 24,177–24,194, 1999.

McCleese, D.J., Schofield, J.T., Taylor, F.W., Abdou, W.A., Aharonson, O., Banfield, D., Calcutt, S.B., Heavens, N.G., Irwin, P.G.J., Kass, D.M., Kleinböhl, A., Lawson, W.G., Leovy, C.B., Lewis, S.R., Paige, D.A., Read, P.L., Richardson, M.I., Teanby, N., Zurek, R.W.: Intense polar temperature inversion in the middle atmosphere on Mars, Nature Geoscience, 1, 745–749, 2008.

Medvedev, A. S., E. Yigit, and P. Hartough, Effects of Gravity Waves Drag in the Martian Atmosphere; Simulations with as GCM, Mars Modeling and Observations Workshop, Extended Abstracts, 374–375, Paris, France, 8–11 February, 2011.

McDunn, T., S. W. Bougher, J. Murphy, M. D. Smith, F. Forget, J.-L.Bertaux, and F. Montmessin, Simulating the Density and Thermal Structure of the Middle Atmosphere (~80–130 km) of Mars Using the MGCM-MTGCM: A Comparison with MEX-SPICAM Observations, Icarus, 206, 5–17, doi:10.1016/j.icarus.2009.06.034, 2010.

Offermann, D., Grossmann, K.U., Barthol, P., Knieling, P., Riese, M., and Trant R.: Cryogenic Infrared Spectrometers and Telescopes for the Atmosphere (CRISTA) experiment and middle atmosphere variability, J. Geophys. Res., 104, 16,311–16,325, 1999.

Pearl, J. C., M. D. Smith, B. J. Conrath, J. L. Bandfield, and P. R. Christensen, Observations of water-ice clouds by the Mars Global Surveyor Thermal Emission Spectrometer experiment: The first martian year, J. Geophys. Res., 12,325-312,338, 2001.

Pollock, D. S., G.B.I.Scott and L.F. Phillips, Rate constant for quenching of $CO_2(010)$ by atomic oxygen, Geophys. Res. Lett., 20, 727–729, 1993.

Quemerais, E., Bertaux, J.-L., Korablev, O., Dimarellis, E., Cot, C., Sandel, B.R., Fussen, D.: Stellar occultations observed by SPICAM on Mars Express, J. Geophys. Res., 111(E09S04), doi:10.1029/2005JE002604, 2006.

Ratkowski, A. J., et al., Lower-thermospheric infra-red emissions from minor species during high-latitude twilight–B. Analysis of 15 μm emission and comparison with non-LTE models, J. Atm. Terr. Phys., 56, 1899–1914, 1994.

Rezac, L., Simultaneous retrieval of T(p) and CO_2 volume mixing ratio from limb observations of infrared radiance under non-LTE conditions, Ph.D. thesis, Hampton University of Virginia, 163 pp, 2011.

Rothman, L.S., D. Jacquemart, A. Barbe, D.C. Benner, M. Birk, L.R. Brown, et al., The HITRAN 2004 molecular spectroscopic database. J. Quant. Spect. Rad. Transf., 96, 139-204, 2005.

Russell III, J. M., M.G. Mlynczak, L.L. Gordley, J. J. Tansock, and R. Esplin, Overview of the SABER experiment and preliminary calibration results, Proc. SPIE, Opt. Spectr. Tech. and Instrum. for Atm. and Space Res. III, 3756, 277–288, 1999.

Rybicki, G. B. and Hummer, D. G.: An accelerated lambda iteration method for multilevel radiative transfer. I - Non-overlapping lines with background continuum, Astron.Astrophys., 245, 171–181, 1991.

Sharma, R. D., and P. P. Wintersteiner, Role of carbon dioxide in cooling planetary thermospheres, Geophys. Res. Lett., 17, 2201–2204, 1990.

Smith, M. D., J. C. Pearl, B. J. Conrath, and P. R. Christensen, Thermal Emission Spectrometer results: Mars atmospheric thermal structure and aerosol distribution, J. Geophys. Res., 106, 23929-23945, 2001.

Smith, M. D., The annual cycle of water vapor on Mars as observed by the Thermal Emission Spectrometer, J. Geophys. Res., 197, 5115, doi:5110.1029/2001JE001522, 2002.

Smith, M. D., Interannual variability in TES atmospheric observations of Mars during 1999-2003, Icarus, 167, 148-165, 2004.

Wolff, M.J., and R.T. Clancy. Constraints on the size of Martian aerosols from Thermal Emission Spectrometer observations. J. Geophys. Res., 108, doi:10.1029/2003JE002057, 2003.

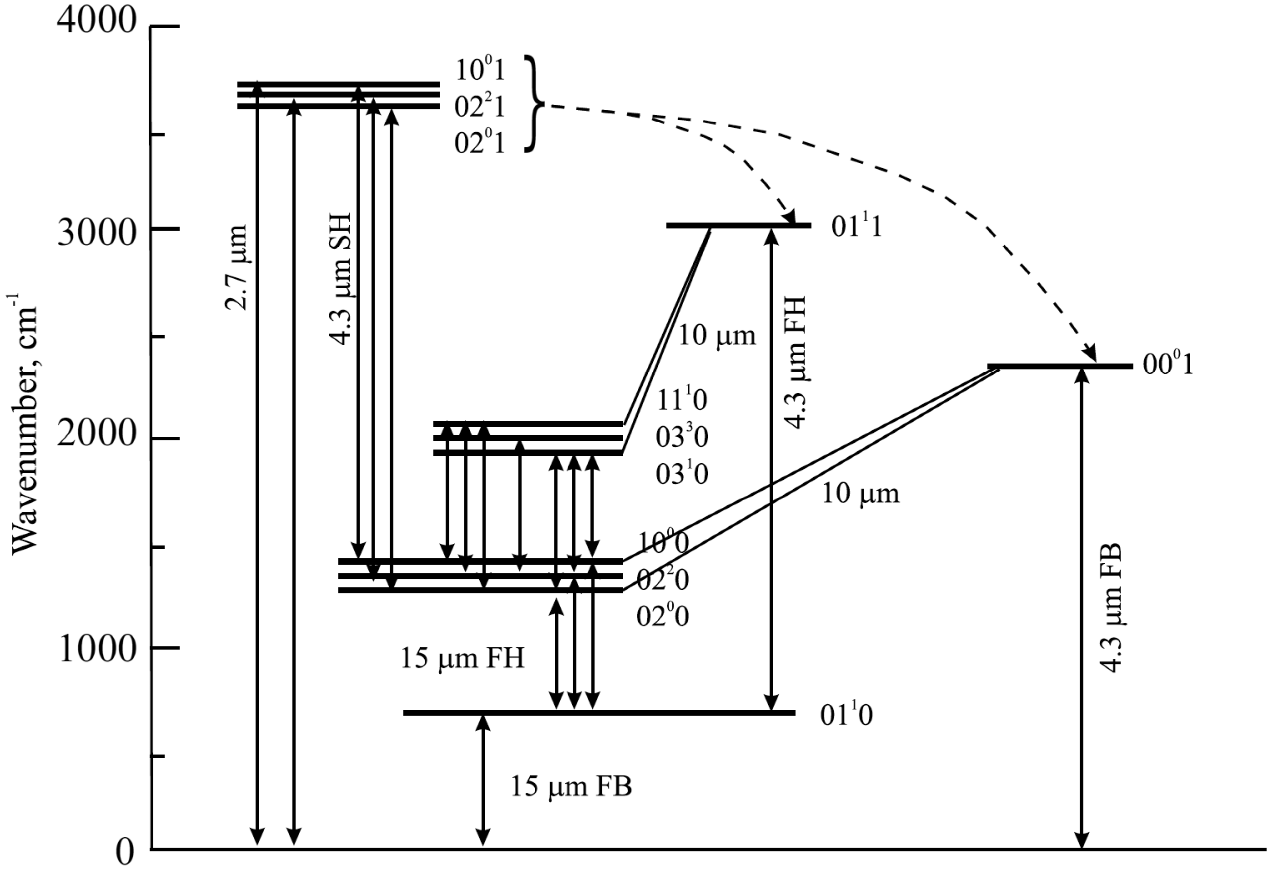

Fig. 1. Scheme of vibrational level and major energy exchange processes for CO_2 and its isotopes. Solid lines: radiative transitions, dashed lines: V–V energy transfer from solar pumped levels. V–T processes are not shown. FB: fundamental band; FH: first hot band; SH: second hot band.

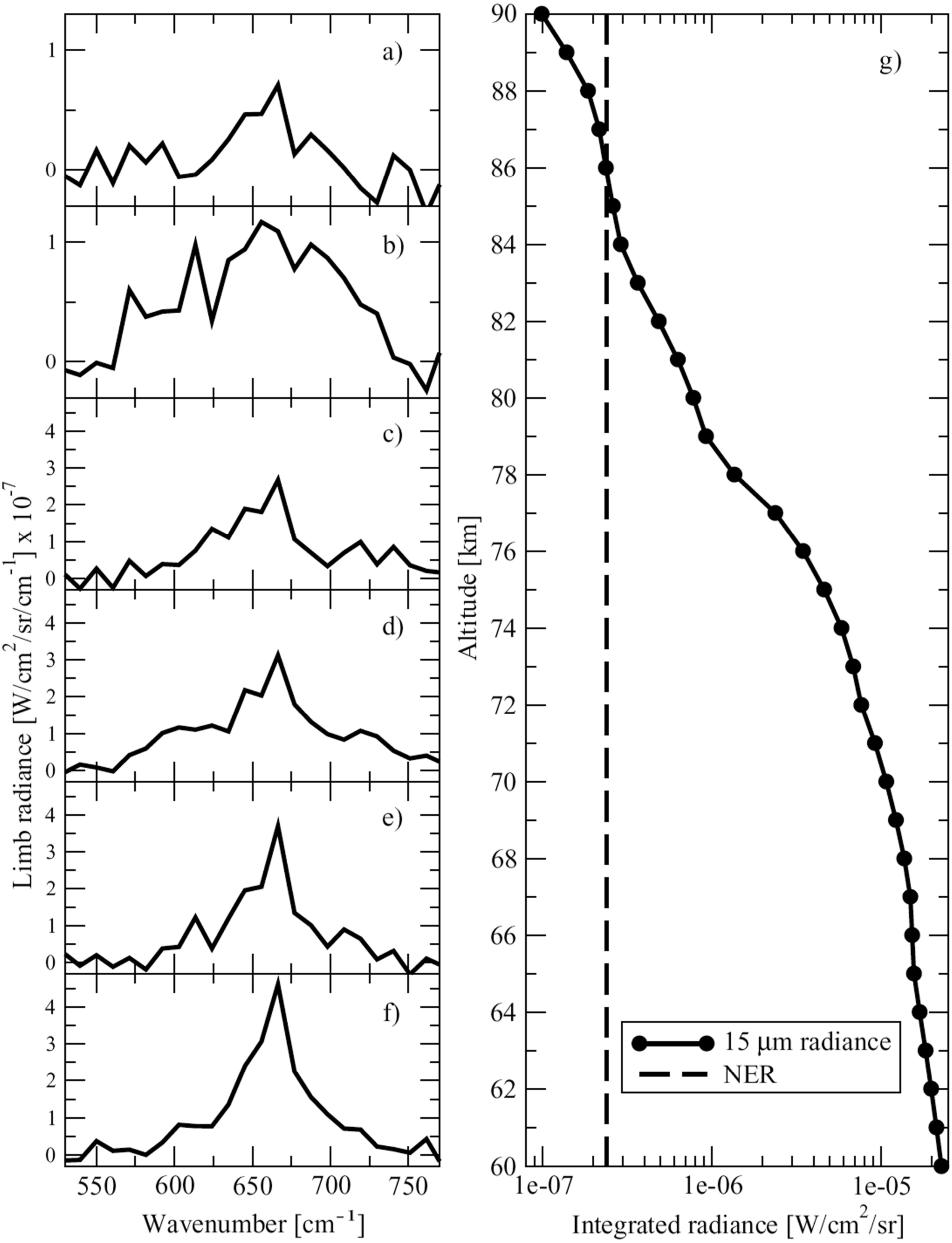

Fig. 2. MGS TES spectra over 530–770 cm^{-1} at: a) 88.6 km; b) 82.6 km; c) 75.6 km; d) 71.4 km; e) 68.2 km; f) 60.8 km. Panel g) shows the 15 μm radiance integrated over the 560–772 cm^{-1} spectral range. Noise equivalent radiance (NER) was estimated from the points outside the integration interval: 508–560 cm^{-1} and 772–825 cm^{-1}.

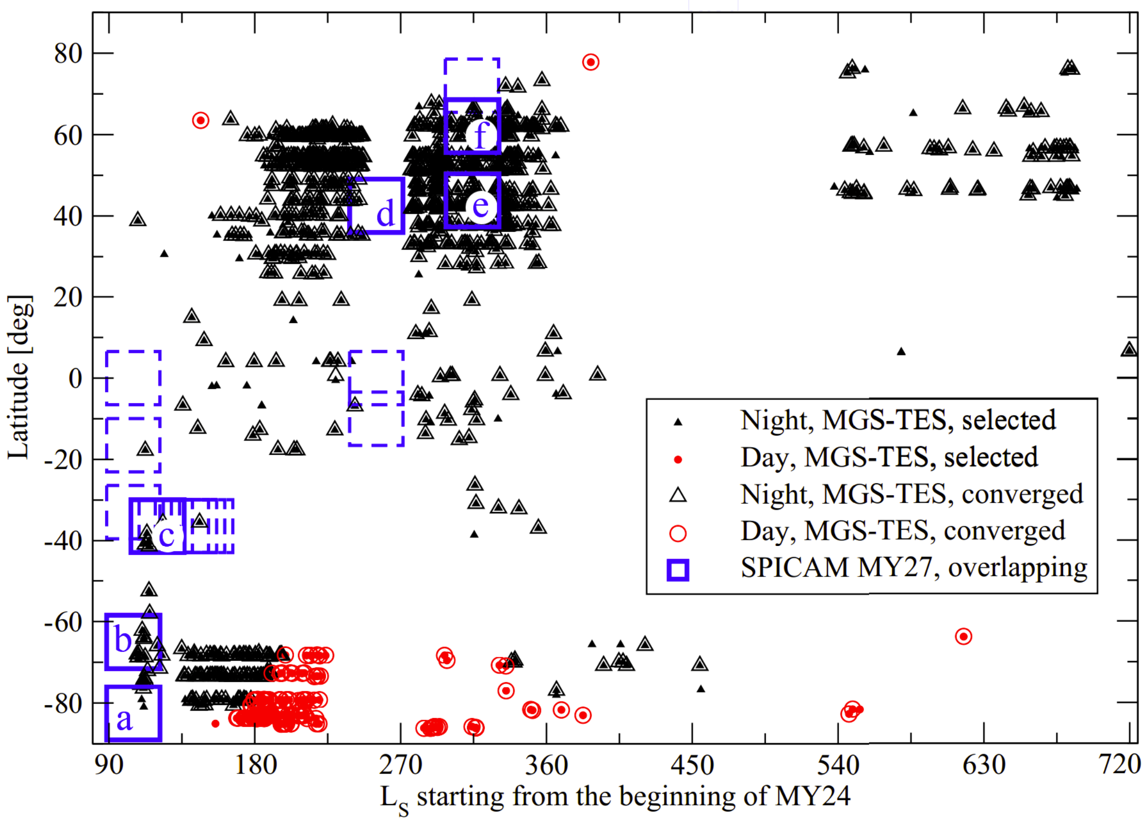

Fig. 3. Seasonal and latitudinal coverage of the MGS TES limb sequences used in this work. Circles: daytime observations. Triangles: nighttime observations. Filled small circles and triangles: observations satisfying the selection criteria. Empty big circles and triangles: observations for which the retrieval algorithm converged. Small rectangles with dashed outline: SPICAM observations for MY27; rectangles with solid outline and a letter: SPICAM observations for MY27 overlapping with TES retrievals and selected for intercomparison in Fig. 8.

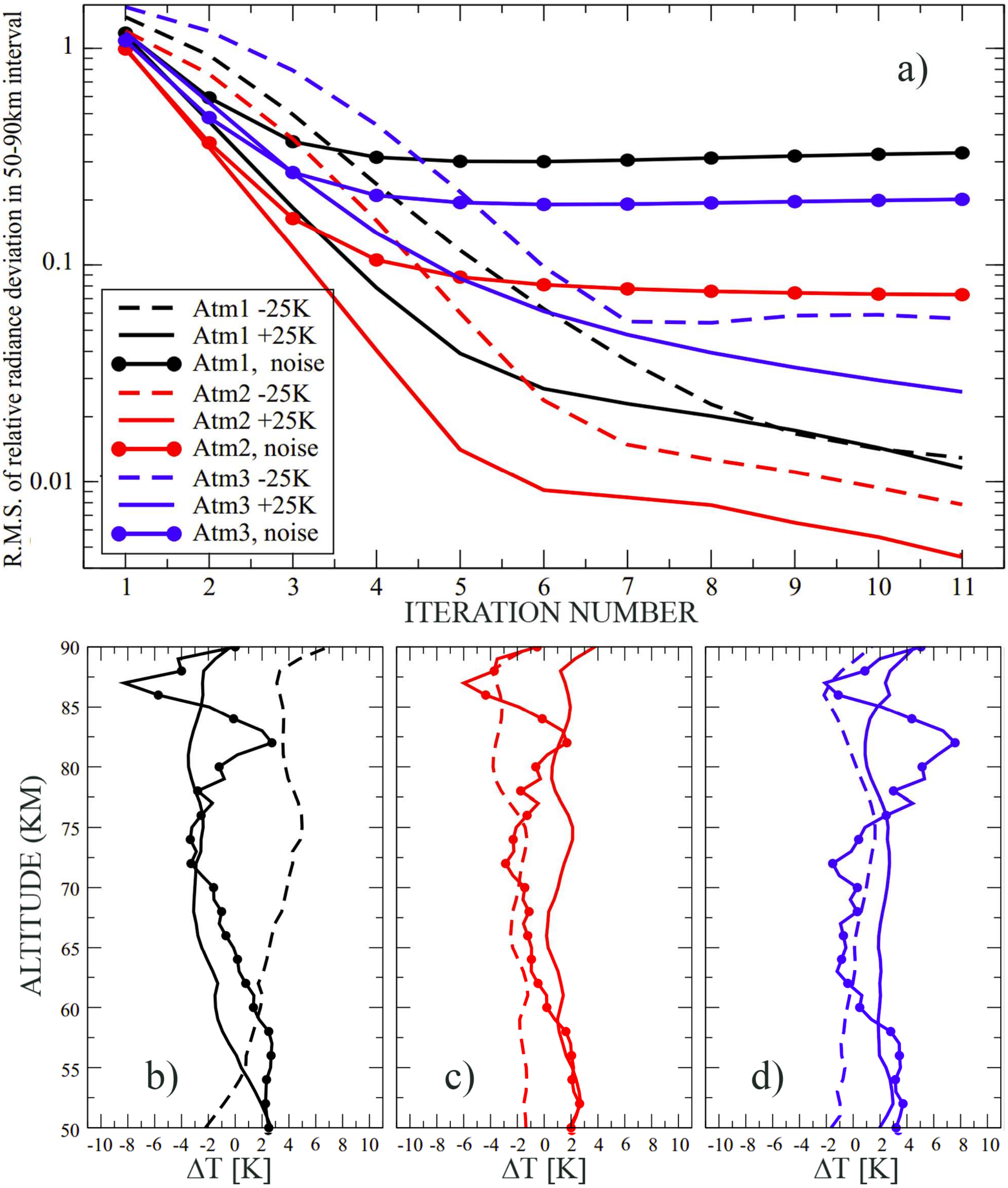

Fig. 4. Self-consistent retrievals for the temperature profiles measured by MCS (Kleinböhl et al., 2009) with GW-perturbation applied: a) convergence of the method for the noise-free retrievals (solid and dashed curves) and retrievals with added noise (solid lines with circles); b)–d): temperature errors for the retrievals starting with 25 K warmer/colder temperature profile (solid and dashed curves, respectively), and for the 25 K warmer temperature profile with added noise.

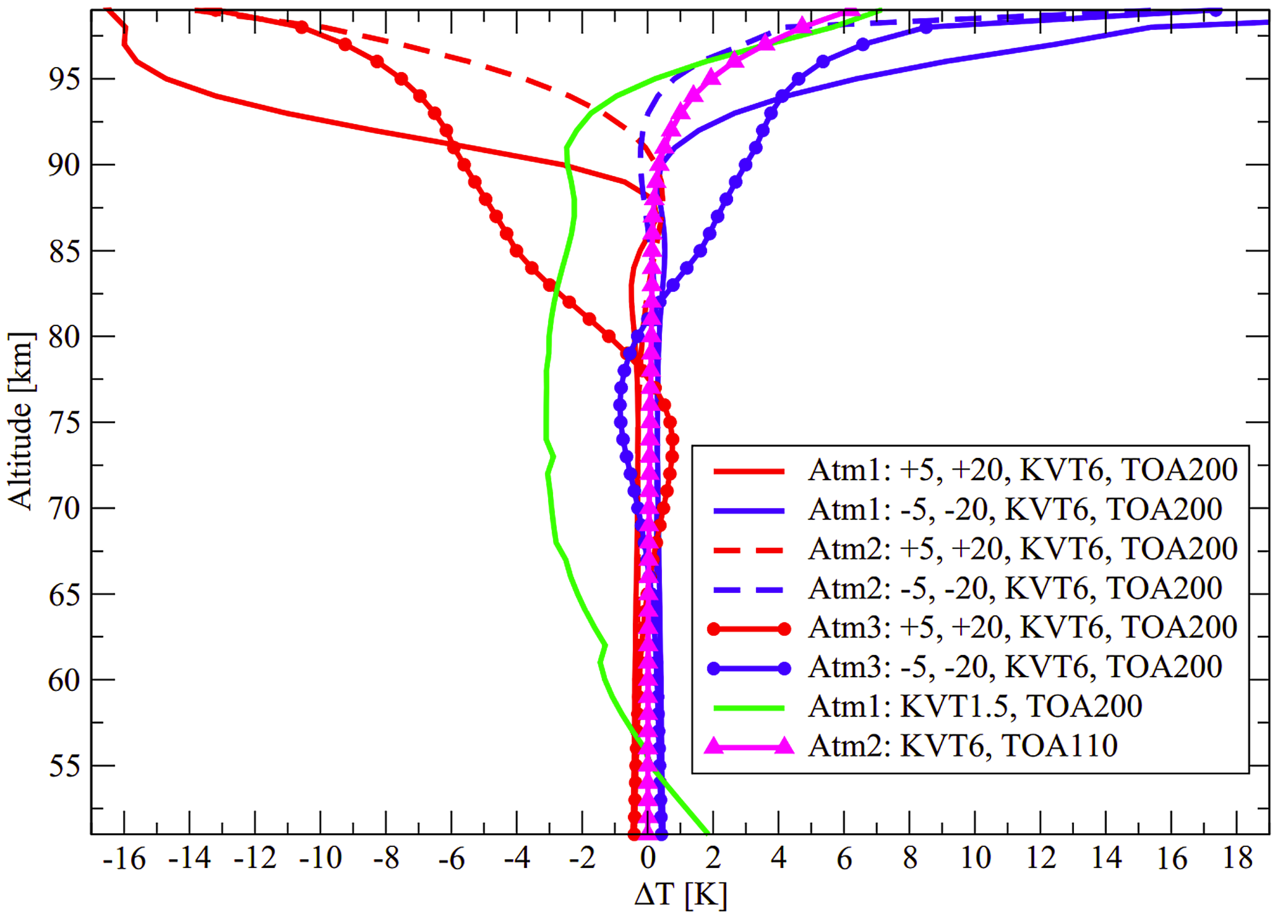

Fig. 5. Sensitivity of temperature retrievals to changes in temperature profile below and above the retrieval range, to $k_{VT}\{CO_2\text{-}O\}$ variations, and to top of atmosphere changes. The retrieved temperature profiles are compared to the "reference" one: no modification of temperature profile, top of atmosphere (TOA) at 200 km, $k_{VT}\{CO_2\text{-}O\}=6\cdot10^{-12}cm^3s^{-1}$. The reference profile was used to obtain reference 15 μm CO_2 radiance profile. Test atmospheres #1,2,3 are described in text. The first value in the legend refers to temperature profile change below 50 km altitude while the second value represents temperature profile shift above 100 km. KVT1.5 corresponds to retrieval performed with $k_{VT}\{CO_2\text{-}O\}=1.5\cdot10^{-12}cm^3s^{-1}$.

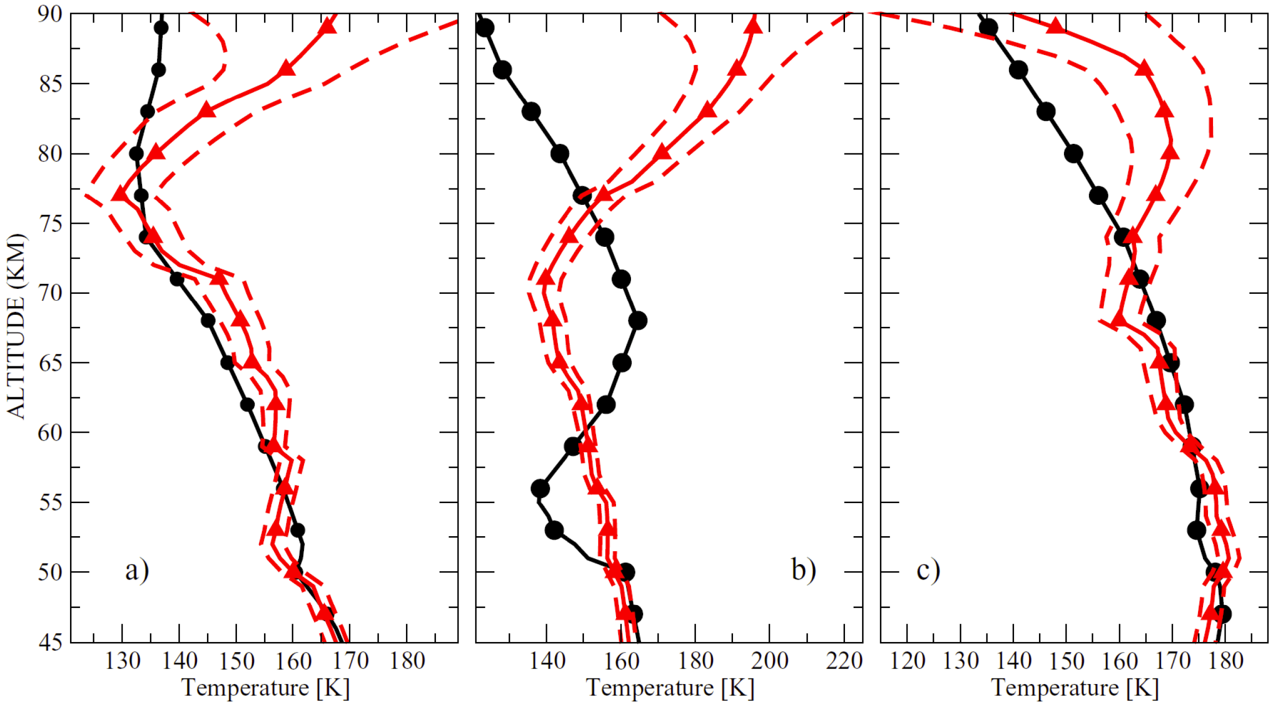

Fig. 6. Temperature retrieval examples: a) L_s=110°, lat = 62S; b) L_s=135°, lat = 6S; c) L_s=180°, lat = 59N. Curves with circles: initial temperature profile (TES below 50 km; MCD above 50 km). Curves with triangles: temperature retrievals performed in this work. Dashed lines: error bars for temperature retrievals.

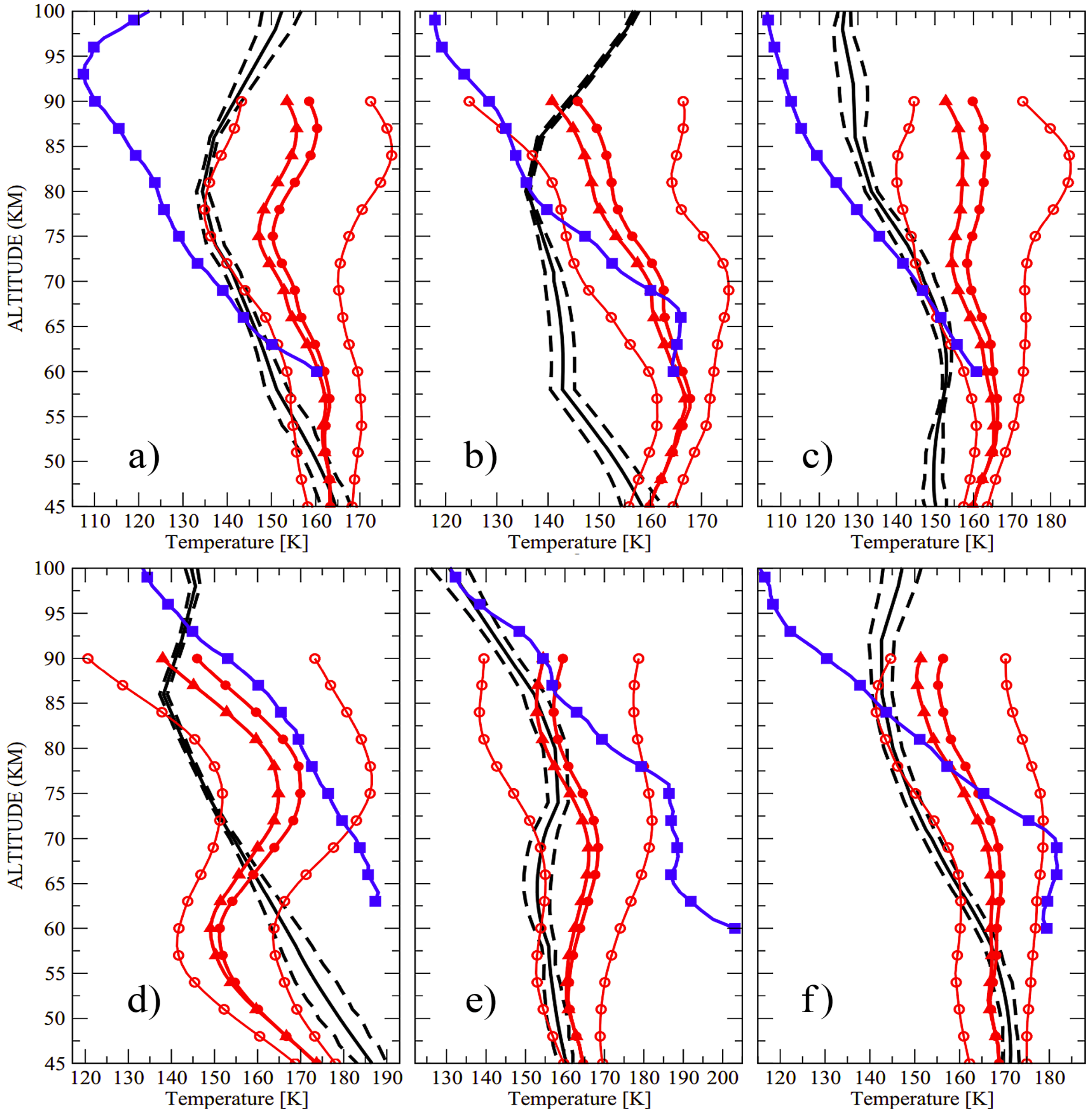

Fig. 7. Comparing TES temperatures (this work) with SPICAM MY27 temperature distributions (Forget et al., 2009) for areas a)–f) defined in Fig. 3 and with MCD simulations. Solid lines: MCD; dashed lines: MCD standard deviations for given latitude and season; lines with filled circles: averaged TES retrievals (this work); lines with empty circles: TES profiles standard deviations (see text and Fig. 6 for TES error bars); lines with triangles: TES profile corrected for high SNR scan selection (see text); lines with filled squares: SPICAM retrievals (Forget et al., 2009): a) L_s = 90–120°, lat= 60S–70S, 9 profiles, 5 K compensation for high SNR selection; b) L_s =90–120°, lat=70S–80S, 7 profiles, 5 K; c) L_s =110–130°, lat = 31S–41S, 4 profiles, 7 K; d) L_s =240–270°, lat = 30N–55N, 23 profiles, 8 K; e) L_s =309–319°, lat =30N–55N, 43 profiles, 5 K; f) L_s =309–319°, lat =57N–67N, 9 profiles, 5 K.

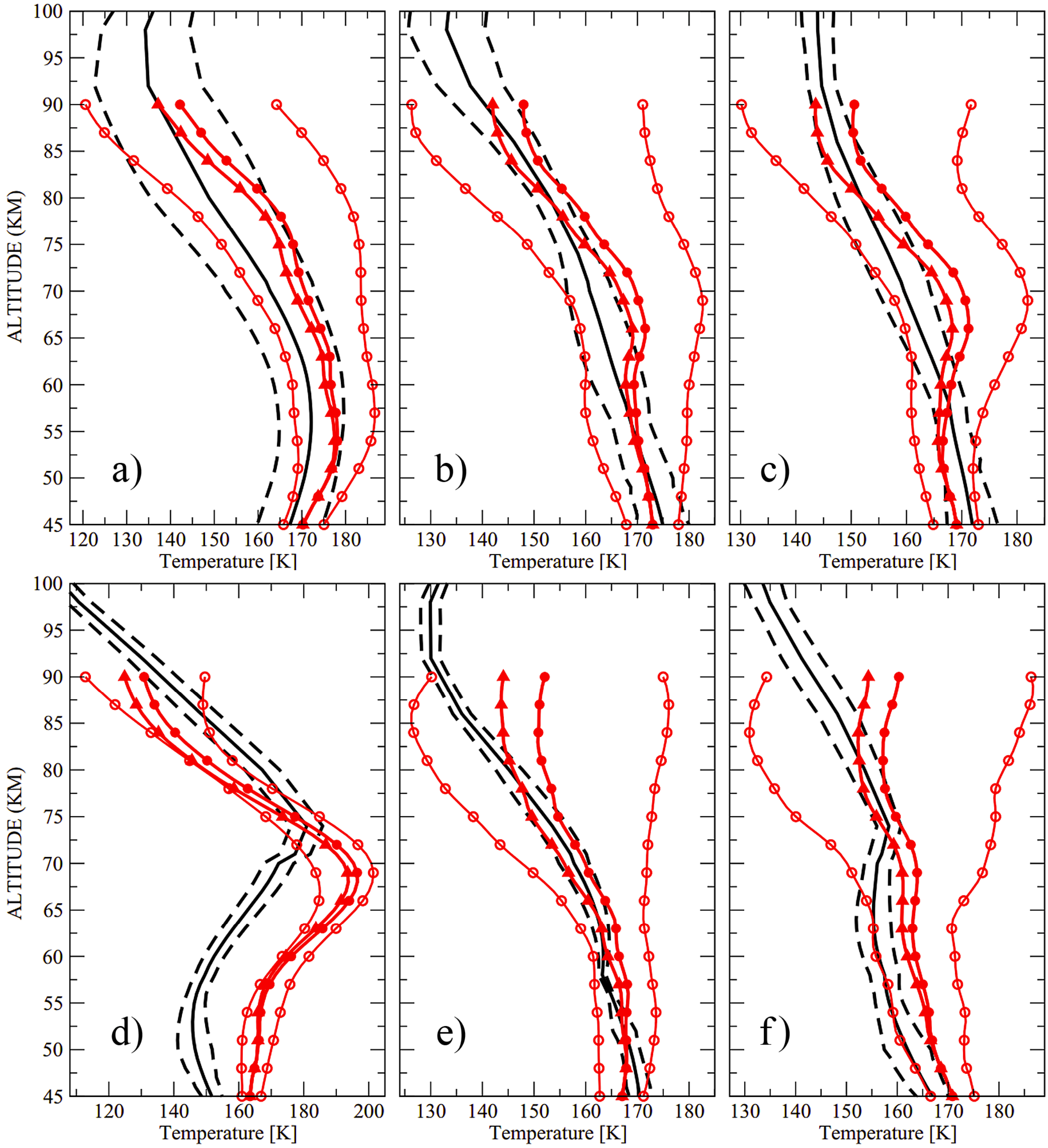

Fig. 8. Same as in Fig. 7 but only for TES versus MCD profiles comparison: a) L_s=165–195°, lat = 65–75S, 49 profiles, 5 K compensation for high SNR selection; b) L_s= 180–225°, lat = 50–65N, 150 profiles, 6 K; c) L_s=285–315°, lat = 55–65N, 25 profiles, 7 K; d) L_s= 345–375°, lat = 20S–20N, 5 profiles, 6 K; e) L_s= 345–375°, lat = 55–65N, 16 profiles, 8 K; f) L_s= 650–685, lat = 40–55N, 14 profiles, 6 K.